A Cartesian grid technique based on one-dimensional integrated radial basis function networks for natural convection in concentric annuli

N. Mai-Duy[*],   K. Le-Cao and T. Tran-Cong

Computational Engineering and Science Research Centre

Faculty of Engineering and Surveying,

The University of Southern Queensland, Toowoomba, QLD 4350, Australia

[*]Corresponding author: Telephone +61 7 4631 1324, Fax +61 7 4631 2526, E-mail maiduy@usq.edu.au

Abstract This paper reports a radial-basis-function (RBF)-based Cartesian grid technique for the simulation of two-dimensional buoyancy-driven flow in concentric annuli. The continuity and momentum equations are represented in the equivalent stream function formulation that reduces the number of equations from three to one, but involves higher-order derivatives. The present technique uses a Cartesian grid to discretize the problem domain. Along a grid line, one-dimensional integrated RBF networks (1D-IRBFNs) are employed to represent the field variables. The capability of 1D-IRBFNs to handle unstructured points with accuracy is exploited to describe non-rectangular boundaries in a Cartesian grid, while the method's ability to avoid the reduction of convergence rate caused by differentiation is instrumental in improving the quality of the approximation of high-order derivatives. The method is applied to simulate thermally-driven flows in annuli between two circular cylinders and between an outer square cylinder and an inner circular cylinder. High Rayleigh-number solutions are achieved and they are in good agreement with previously published numerical data.

1   Introduction

Natural convection has been of great interest in many fields of science and engineering such as meteorology, nuclear reactors and solar energy systems. The problem has been extensively studied by both experimental and numerical simulations. For the latter, one needs to find a numerical solution of a set of partial differential equations (PDEs), namely the continuity, conservation of momentum and conservation of energy. Such a numerical solution can be achieved by means of

2

discretization schemes, followed by algebraic equations solution. Numerical simulations of buoyancy-driven flow have been conducted by a variety of numerical techniques such as finite-difference methods (FDMs) (e.g. [1,2]), finite-element methods (FEMs) (e.g. [3,4]), finite-volume methods (FVMs) (e.g. [5,6]), boundary-element methods (BEMs) (e.g. [7-9]) and spectral techniques (e.g. [10,11]). It is noted that natural convection heat transfer in a square slot is considered as a benchmark test problem for the assessment of new numerical solvers in CFD.

The objective of discretization techniques is to reduce the PDEs to sets of algebraic equations. To do so, the problem domain needs to be discretized into a set of finite elements (e.g. [3,4]), a Cartesian grid (e.g. [1,2]) or a set of unstructured points (e.g. [12,13]). Among these typical types of domain discretization, generating a Cartesian grid can be seen to be the most straightforward task. There has been a renewed interest in the development of Cartesian-grid-based techniques for dealing with problems defined in geometrically-complicated domains (e.g. [14-19]).

Over the last fifteen years, the RBF collocation methods have emerged as an attractive solver for PDEs. The methods are extremely easy to use and capable of achieving a high degree of accuracy using relatively low numbers of nodal points. They have been successful to solve different types of differential problems encountered in applied mathematics, science and engineering (e.g. [20-25]). However, there is still a lack of mathematical theories for specifying optimal values of the free parameters of the RBF. The obtained system matrix is fully populated and its condition number grows rapidly as the number of nodes is increased. As a result, in practice, one has great difficulty making full use of the capabilities of the RBF method. Very recently, an efficient RBF technique based on 1D-IRBF approximation schemes and Cartesian grids for linear elliptic problems in irregular domains has been reported in [26]. The problem domain is simply embedded in a Cartesian grid. The RBF approximations at a grid node involve only points that lie on the

3

grid lines intersected at that point rather than the whole set of nodes, leading to a significant improvement in the matrix condition number and computational effort. Moreover, the construction of the RBF approximations is based on integration (the integral collocation approach), and therefore avoids the reduction of convergence rate caused by differentiation. The 1D-IRBF technique allows a larger number of nodes to be employed. Numerical results have shown that it yields a fast rate of convergence with grid refinement.

In this paper, we extend a 1D-IRBFN-based Cartesian grid technique to the simulation of buoyancy-driven flow defined in a multiply-connected domain and governed by a set of nonlinear PDEs. The motion of a fluid is caused by the combination of density variations and gravity. The velocity and temperature fields are closely coupled. At high values of the Rayleigh number, very thin boundary layers are formed, making the numerical simulation difficult. The traditional FDM (e.g. [1]) and differential-quadrature technique (DQM) (e.g. [11,27]) require the computational domains be rectangular. Coordinate transformations are thus employed. Subsequently, the governing equations are transformed into the new forms that are usually more complicated. The relationships between the physical and computational coordinates are given by a set of algebraic equations or a set of PDEs, depending on the level of complexity of the geometry. In contrast, the present technique succeeds in retaining the Cartesian form of the governing equations. Furthermore, they are written in terms of stream function and temperature. This equivalent formulation reduces the number of dependent variables from four (two velocity components, pressure and temperature) to two (stream function and temperature). However, the formulation's well-known drawback is that the obtained system involves higher-order derivatives and double boundary conditions. It will be shown that such difficulties can be handled effectively with the present integral collocation approach.

The remainder of the paper is organized as follows. Section 2 gives a brief review of

the governing equations, focusing on the stream function-temperature formulation. The 1D-IRBFN-based Cartesian grid technique is presented in section 3. The present method is applied to simulate natural convection in annuli between two circular cylinders and between an outer square cylinder and an inner circular cylinder in section 4. Section 5 gives some concluding remarks.

2 Governing equations

Using the Boussinesq approximation, the 2D dimensionless forms of the governing equations for buoyancy-driven flow can be written as (e.g. [28])

$$\frac{\partial u}{\partial x} + \frac{\partial v}{\partial y} = 0, \tag{1}$$

$$\frac{\partial u}{\partial t} + u\frac{\partial u}{\partial x} + v\frac{\partial u}{\partial y} = -\frac{\partial p}{\partial x} + \sqrt{\frac{Pr}{Ra}}\left(\frac{\partial^2 u}{\partial x^2} + \frac{\partial^2 u}{\partial y^2}\right), \tag{2}$$

$$\frac{\partial v}{\partial t} + u\frac{\partial v}{\partial x} + v\frac{\partial v}{\partial y} = -\frac{\partial p}{\partial y} + \sqrt{\frac{Pr}{Ra}}\left(\frac{\partial^2 v}{\partial x^2} + \frac{\partial^2 v}{\partial y^2}\right) + T, \tag{3}$$

$$\frac{\partial T}{\partial t} + u\frac{\partial T}{\partial x} + v\frac{\partial T}{\partial y} = \frac{1}{\sqrt{RaPr}}\left(\frac{\partial^2 T}{\partial x^2} + \frac{\partial^2 T}{\partial y^2}\right), \tag{4}$$

where u and v are the velocity components, p the dynamic pressure, T the temperature, and Pr and Ra the Prandtl and Rayleigh numbers defined as $Pr = \nu/\alpha$ and $Ra = \beta g \Delta T L^3/\alpha\nu$, respectively in which ν is the kinematic viscosity, α the thermal diffusivity, β the thermal expansion coefficient, g the gravity, and L and ΔT the characteristic length and temperature difference, respectively. In this dimensionless scheme, the velocity scale is taken as $U = \sqrt{gL\beta\Delta T}$ for the purpose of balancing the buoyancy and inertial forces.

5

By writing the velocity components in terms of a stream function ψ defined as

$$u = \frac{\partial \psi}{\partial y}, \quad v = -\frac{\partial \psi}{\partial x},$$

the continuity equation is satisfied identically and the momentum equations reduce to

$$\frac{\partial}{\partial t}\left(\frac{\partial^2 \psi}{\partial x^2} + \frac{\partial^2 \psi}{\partial y^2}\right) + \frac{\partial \psi}{\partial y}\left(\frac{\partial^3 \psi}{\partial x^3} + \frac{\partial^3 \psi}{\partial x \partial y^2}\right) - \frac{\partial \psi}{\partial x}\left(\frac{\partial^3 \psi}{\partial x^2 \partial y} + \frac{\partial^3 \psi}{\partial y^3}\right) =$$
$$\sqrt{\frac{Pr}{Ra}}\left(\frac{\partial^4 \psi}{\partial x^4} + 2\frac{\partial^4 \psi}{\partial x^2 \partial y^2} + \frac{\partial^4 \psi}{\partial y^4}\right) - \frac{\partial T}{\partial x}. \tag{5}$$

Using the equivalent stream function formulation, the set of four equations (1)-(4) reduces to a set of two equations: (4) and (5).

The boundary conditions on (u, v) can be converted into the boundary conditions on stream function and its normal derivative, namely

$$\psi = f \quad \text{and} \quad \frac{\partial \psi}{\partial n} = g,$$

where f and g are prescribed functions and n is the direction normal to the boundary.

3 The proposed technique

3.1 One-dimensional IRBFNs

RBFNs are known as a universal approximator. The RBFN allows the conversion of a function to be approximated from a low-dimensional space to a high-dimensional

space in which the function is expressed as a linear combination of RBFs

$$f(x) = \sum_{i=1}^{m} w_i g_i(x), \tag{6}$$

where m is the number of RBFs, $\{g_i(x)\}_{i=1}^{m}$ the set of RBFs, and $\{w_i\}_{i=1}^{m}$ the set of weights to be found.

In the traditional/direct approach, a function f is approximated by an RBFN, followed by successive differentiations to obtain approximate expressions for its derivatives. There is a reduction in convergence rate for derivative functions and this reduction is an increasing function of derivative order [29].

Mai-Duy and Tran-Cong [24,30] have proposed the use of integration to construct the RBF approximations. A derivative of f is decomposed into RBFs, and lower-order derivatives and the function itself are then obtained through integration

$$\frac{d^p f(x)}{dx^p} = \sum_{i=0}^{m} w_i g_i(x) = \sum_{i=0}^{m} w_i I_i^{(p)}(x), \tag{7}$$

$$\frac{d^{p-1} f(x)}{dx^{p-1}} = \sum_{k=0}^{m} w_i I_i^{(p-1)}(x) + c_1, \tag{8}$$

$$\frac{d^{p-2} f(x)}{dx^{p-2}} = \sum_{k=0}^{m} w_i I_i^{(p-2)}(x) + c_1 x + c_2, \tag{9}$$

$$\cdots \quad \cdots \quad \cdots \quad \cdots \quad \cdots$$

$$\frac{df(x)}{dx} = \sum_{k=0}^{m} w_i I_i^{(1)}(x) + c_1 \frac{x^{p-2}}{(p-2)!} + c_2 \frac{x^{p-3}}{(p-3)!} + \cdots + c_{p-2} x + c_{p-1}, \tag{10}$$

$$f(x) = \sum_{k=0}^{m} w_i I_i^{(0)}(x) + c_1 \frac{x^{p-1}}{(p-1)!} + c_2 \frac{x^{p-2}}{(p-2)!} + \cdots + c_{p-1} x + c_p, \tag{11}$$

where $I_i^{(p-1)}(x) = \int I_i^{(p)}(x) dx$, $I_i^{(p-2)}(x) = \int I_i^{(p-1)}(x) dx, \cdots, I_i^{(0)}(x) = \int I_i^{(1)}(x) dx$, and $c_1, c_2, \cdots, c_p$ are the constants of integration. Numerical results have shown that the integral approach significantly improves the quality of the approximation

7

of derivative functions over conventional differential approaches. The IRBF approx-
imation scheme is said to be of pth-order, denoted by IRBFN-p, if the pth-order
derivative is taken as the staring point.

It has generally been accepted that, among RBFs, the multiquadric (MQ) scheme
tends to result in the most accurate approximation. The present technique imple-
ments the MQ function whose form is

$$g_i(x) = \sqrt{(x - c_i)^2 + a_i^2}, \qquad (12)$$

where c_i and a_i are the centre and the width of the ith basis function.

3.2   Simulation of buoyancy-driven flow

Consider the process of natural convection between two cylinders, one heated and the
other cooled (e.g. Figure 1). The problem domain is discretized using a Cartesian
grid with a grid spacing h. Grid points outside the domain (external points) together
with internal points that fall very close–within a distance of $h/8$–to the boundary
are removed. The remaining grid points are taken to be the interior nodes. The
boundary nodes consists of the grid points that lie on the boundaries, and points
that are generated by the intersection of the grid lines with the boundaries.

Along each grid line, 1D-IRBFNs are employed to discretize the solution and its
relevant derivatives. In what follows, the proposed method is presented in detail for
the energy equation (4) and the momentum equation (5). Special attention is given
to the implementation of boundary conditions.

3.2.1 IRBFN discretization of the energy equation

The energy equation involves the following linear second-order differential operator

$$\mathcal{L}_2 = \frac{\partial^2}{\partial x^2} + \frac{\partial^2}{\partial y^2}. \tag{13}$$

As presented earlier, an IRBFN-p scheme permits the approximation of a function and its derivatives of orders up to p. To use integrated basis functions only, one needs to employ IRBFNs of at least second order. A line in the grid contains two sets of points (Figure 2). The first set consists of the interior points that are also the grid nodes (regular nodes). The values of the temperature at the interior points are unknown. The second set is formed from the boundary nodes that do not generally coincide with the grid nodes (irregular nodes). At the boundary nodes, the values of the temperature are given.

For the classical FDM, the irregular points require changes of Δx and Δy in the formulas, and such changes deteriorate the order of truncation error (e.g. [31]).

Unlike the finite-difference and spectral approximation schemes, the IRBFNs have the capability to handle unstructured points with high accuracy. This approximation power will be exploited here to implement the boundary conditions. The boundary conditions are imposed through the process of converting the network-weight space into the physical space (conversion process).

Consider a horizontal grid line (Figure 2). An important feature of the present technique is that, along the grid line, both interior points $\{x_i\}_{i=1}^q$ and boundary points $\{x_{bi}\}_{i=1}^2$ are taken to be the centres of the network. This work employs 1D-IRBFN-2s to discretize the temperature field T. The conversion system is constructed as

follows

$$\begin{pmatrix} \widehat{T} \\ \widehat{T}_b \end{pmatrix} = \widehat{\mathcal{C}} \, \widehat{w}, \tag{14}$$

where

$$\widehat{T} = (T_1, T_2, \cdots, T_q)^T,$$

$$\widehat{T}_b = (T_{b1}, T_{b2})^T,$$

$$\widehat{w} = (w_1, w_2, \cdots, w_m, c_1, c_2)^T,$$

$$\widehat{\mathcal{C}} = \begin{bmatrix} I_1^{(0)}(x_1) & \cdots & I_m^{(0)}(x_1) & x_1 & 1 \\ I_1^{(0)}(x_2) & \cdots & I_m^{(0)}(x_2) & x_2 & 1 \\ \cdots & \cdots & \cdots & \cdots & \cdots \\ I_1^{(0)}(x_q) & \cdots & I_m^{(0)}(x_q) & x_q & 1 \\ I_1^{(0)}(x_{b1}) & \cdots & I_m^{(0)}(x_{b1}) & x_{b1} & 1 \\ I_1^{(0)}(x_{b2}) & \cdots & I_m^{(0)}(x_{b2}) & x_{b2} & 1 \end{bmatrix},$$

and $m = q + 2$.

The obtained system (14) for the unknown vector of network weights can be solved using the singular value decomposition (SVD) technique

$$\widehat{w} = \widehat{\mathcal{C}}^{-1} \begin{pmatrix} \widehat{T} \\ \widehat{T}_b \end{pmatrix}, \tag{15}$$

where $\widehat{\mathcal{C}}^{-1}$ is the Moore-Penrose pseudoinverse and $\widehat{w}$ is the minimal norm solution.

Taking (15) into account, the values of the first and second derivatives of T at the

interior points are computed by

$$
\begin{pmatrix}
\frac{\partial T_1}{\partial x} \\
\frac{\partial T_2}{\partial x} \\
\vdots \\
\frac{\partial T_q}{\partial x}
\end{pmatrix}
=
\begin{bmatrix}
I_1^{(1)}(x_1) & \cdots & I_m^{(1)}(x_1) & 1 & 0 \\
I_1^{(1)}(x_2) & \cdots & I_m^{(1)}(x_2) & 1 & 0 \\
\cdots & \cdots & \cdots & \cdots & \cdots \\
I_1^{(1)}(x_q) & \cdots & I_m^{(1)}(x_q) & 1 & 0
\end{bmatrix}
\widehat{\mathcal{C}}^{-1}
\begin{pmatrix}
\widehat{T} \\
\widehat{T}_b
\end{pmatrix},
\tag{16}
$$

and

$$
\begin{pmatrix}
\frac{\partial^2 T_1}{\partial x^2} \\
\frac{\partial^2 T_2}{\partial x^2} \\
\vdots \\
\frac{\partial^2 T_q}{\partial x^2}
\end{pmatrix}
=
\begin{bmatrix}
I_1^{(2)}(x_1) & \cdots & I_m^{(2)}(x_1) & 0 & 0 \\
I_1^{(2)}(x_2) & \cdots & I_m^{(2)}(x_2) & 0 & 0 \\
\cdots & \cdots & \cdots & \cdots & \cdots \\
I_1^{(2)}(x_q) & \cdots & I_m^{(2)}(x_q) & 0 & 0
\end{bmatrix}
\widehat{\mathcal{C}}^{-1}
\begin{pmatrix}
\widehat{T} \\
\widehat{T}_b
\end{pmatrix},
\tag{17}
$$

or in compact forms

$$
\widehat{\frac{\partial T}{\partial x}} = \widehat{\mathcal{D}}_{1x}\widehat{T} + \widehat{k}_{1x},
\tag{18}
$$

and

$$
\widehat{\frac{\partial^2 T}{\partial x^2}} = \widehat{\mathcal{D}}_{2x}\widehat{T} + \widehat{k}_{2x},
\tag{19}
$$

where the matrices $\widehat{\mathcal{D}}_{1x}$ and $\widehat{\mathcal{D}}_{2x}$ consist of all but the last two columns of the product of two matrices on the right-hand side of (16) and (17), and $\widehat{k}_{1x}$ and $\widehat{k}_{2x}$ are obtained from multiplying the vector $\widehat{T}_b$ by these last two columns. It is noted that $\widehat{k}_{1x}$ and $\widehat{k}_{2x}$ are the vectors of known quantities related to boundary conditions.

It can be seen from (18) and (19) that the IRBFN approximations of $\partial T/\partial x$ and $\partial^2 T/\partial x^2$ at the interior points include information about the inner and outer boundaries (locations and boundary values). Thus it remains only to force these approximations to satisfy the governing equation.

The incorporation of the boundary points into the set of centres has several advantages:

11

- It allows the two sets of centres and collocation points to be the same, i.e. $\{c_i\}_{i=1}^m \equiv \left\{\{x_i\}_{i=1}^q \cup \{x_{bi}\}_{i=1}^2\right\}$. Numerical investigations [24,32] have indicated that when these two sets coincide, the RBF approximation scheme tends to result in the most accurate numerical solution.

- It allows the use of IRBFNs with a fixed order (IRBFN-2), regardless of the shape of the domain.

In the same manner, one can obtain the IRBF expressions for $\partial T/\partial y$ and $\partial^2 T/\partial y^2$ at the interior points along a vertical line.

As with FDMs, FVMs, BEMs and FEMs, the IRBF approximations will be gathered together to form the global matrices for the discretization of the PDE. By collocating the governing equation at the interior points, a square system of algebraic equations is obtained, which is solved for the approximate temperature at the interior points.

3.2.2 IRBFN discretization of the momentum equation

The momentum equation involves the following linear fourth-order differential operator

$$\mathcal{L}_4 = \frac{\partial^4}{\partial x^4} + 2\frac{\partial^4}{\partial x^2 \partial y^2} + \frac{\partial^4}{\partial y^4}. \tag{20}$$

At each boundary node, the solution is required to satisfy two prescribed values, ψ and $\partial\psi/\partial n$. It is straightforward to obtain the values of $\partial\psi/\partial x$ and $\partial\psi/\partial y$ at the boundary nodes from the prescribed conditions. The double boundary conditions are implemented through the conversion process of the network-weight space into the physical space.

Along each grid line, the set of centres also consists of the interior points and the boundary points. The addition of extra equations to the conversion system for rep-

resenting derivative boundary conditions is offset by the generation of additional unknowns of the integral collocation approach. Consider a horizontal grid line (Figure 2). The present work employs 1D-IRBFN-4s to approximate the variable ψ. The conversion system is given by

$$
\begin{pmatrix}
\widehat{\psi} \\
\widehat{\psi_b} \\
\widehat{\dfrac{\partial \psi_b}{\partial x}}
\end{pmatrix}
= \widehat{\mathcal{C}}\, \widehat{w},
\tag{21}
$$

where

$$\widehat{\psi} = (\psi_1, \psi_2, \cdots, \psi_q)^T,$$

$$\widehat{\psi_b} = (\psi_{b1}, \psi_{b2})^T,$$

$$\frac{\partial \widehat{\psi_b}}{\partial x} = \left(\frac{\partial \psi_{b1}}{\partial x}, \frac{\partial \psi_{b2}}{\partial x} \right)^T,$$

$$\widehat{w} = (w_1, w_2, \cdots, w_m, c_1, c_2, c_3, c_4)^T,$$

$$
\widehat{\mathcal{C}} =
\begin{bmatrix}
I_1^{(0)}(x_1) & \cdots & I_m^{(0)}(x_1) & x_1^3/6 & x_1^2/2 & x_1 & 1 \\
I_1^{(0)}(x_2) & \cdots & I_m^{(0)}(x_2) & x_2^3/6 & x_2^2/2 & x_2 & 1 \\
\cdots & \cdots & \cdots & \cdots & \cdots & & \\
I_1^{(0)}(x_q) & \cdots & I_m^{(0)}(x_q) & x_q^3/6 & x_q^2/2 & x_q & 1 \\
I_1^{(0)}(x_{b1}) & \cdots & I_m^{(0)}(x_{b1}) & x_{b1}^3/6 & x_{b1}^2/2 & x_{b1} & 1 \\
I_1^{(0)}(x_{b2}) & \cdots & I_m^{(0)}(x_{b2}) & x_{b2}^3/6 & x_{b2}^2/2 & x_{b2} & 1 \\
I_1^{(1)}(x_{b1}) & \cdots & I_m^{(1)}(x_{b1}) & x_{b1}^2/2 & x_{b1} & 1 & 0 \\
I_1^{(1)}(x_{b2}) & \cdots & I_m^{(1)}(x_{b2}) & x_{b2}^2/2 & x_{b2} & 1 & 0
\end{bmatrix},
$$

and $m = q + 2$.

The minimal norm solution of (21) can be obtained by the SVD technique

$$
\widehat{w} = \widehat{\mathcal{C}}^{-1}
\begin{pmatrix}
\widehat{\psi} \\
\widehat{\psi}_b \\
\widehat{\frac{\partial \psi_b}{\partial x}}
\end{pmatrix},
\tag{22}
$$

where $\widehat{\mathcal{C}}^{-1}$ is the pseudo-inverse.

The values of the lth-order derivative ($l = \{1, 2, 3, 4\}$) of ψ at the interior points on the line are evaluated as

$$
\begin{pmatrix}
\frac{\partial^4 \psi_1}{\partial x^4} \\
\frac{\partial^4 \psi_2}{\partial x^4} \\
\vdots \\
\frac{\partial^4 \psi_q}{\partial x^4}
\end{pmatrix}
=
\begin{bmatrix}
I_1^{(4)}(x_1) & \cdots & I_m^{(4)}(x_1) & 0 & 0 & 0 & 0 \\
I_1^{(4)}(x_2) & \cdots & I_m^{(4)}(x_2) & 0 & 0 & 0 & 0 \\
\cdots & \cdots & \cdots & \cdots & \cdots \\
I_1^{(4)}(x_q) & \cdots & I_m^{(4)}(x_q) & 0 & 0 & 0 & 0
\end{bmatrix}
\widehat{\mathcal{C}}^{-1}
\begin{pmatrix}
\widehat{\psi} \\
\widehat{\psi}_b \\
\widehat{\frac{\partial \psi_b}{\partial x}}
\end{pmatrix},
\tag{23}
$$

$$
\begin{pmatrix}
\frac{\partial^3 \psi_1}{\partial x^3} \\
\frac{\partial^3 \psi_2}{\partial x^3} \\
\vdots \\
\frac{\partial^3 \psi_q}{\partial x^3}
\end{pmatrix}
=
\begin{bmatrix}
I_1^{(3)}(x_1) & \cdots & I_m^{(3)}(x_1) & 1 & 0 & 0 & 0 \\
I_1^{(3)}(x_2) & \cdots & I_m^{(3)}(x_2) & 1 & 0 & 0 & 0 \\
\cdots & \cdots & \cdots & \cdots & \cdots \\
I_1^{(3)}(x_q) & \cdots & I_m^{(3)}(x_q) & 1 & 0 & 0 & 0
\end{bmatrix}
\widehat{\mathcal{C}}^{-1}
\begin{pmatrix}
\widehat{\psi} \\
\widehat{\psi}_b \\
\widehat{\frac{\partial \psi_b}{\partial x}}
\end{pmatrix},
\tag{24}
$$

$$
\begin{pmatrix}
\frac{\partial^2 \psi_1}{\partial x^2} \\
\frac{\partial^2 \psi_2}{\partial x^2} \\
\vdots \\
\frac{\partial^2 \psi_q}{\partial x^2}
\end{pmatrix}
=
\begin{bmatrix}
I_1^{(2)}(x_1) & \cdots & I_m^{(2)}(x_1) & x_1 & 1 & 0 & 0 \\
I_1^{(2)}(x_2) & \cdots & I_m^{(2)}(x_2) & x_2 & 1 & 0 & 0 \\
\cdots & \cdots & \cdots & \cdots & \cdots \\
I_1^{(2)}(x_q) & \cdots & I_m^{(2)}(x_q) & x_q & 1 & 0 & 0
\end{bmatrix}
\widehat{\mathcal{C}}^{-1}
\begin{pmatrix}
\widehat{\psi} \\
\widehat{\psi}_b \\
\widehat{\frac{\partial \psi_b}{\partial x}}
\end{pmatrix},
\tag{25}
$$

14

and

$$
\begin{pmatrix}
\frac{\partial \psi_1}{\partial x} \\
\frac{\partial \psi_2}{\partial x} \\
\vdots \\
\frac{\partial \psi_q}{\partial x}
\end{pmatrix}
=
\begin{bmatrix}
I_1^{(1)}(x_1) & \cdots & I_m^{(1)}(x_1) & x_1^2/2 & x_1 & 1 & 0 \\
I_1^{(1)}(x_2) & \cdots & I_m^{(1)}(x_2) & x_2^2/2 & x_2 & 1 & 0 \\
\cdots & \cdots & \cdots & \cdots & \cdots \\
I_1^{(1)}(x_q) & \cdots & I_m^{(1)}(x_q) & x_q^2/2 & x_q & 1 & 0
\end{bmatrix}
\widehat{\mathcal{C}}^{-1}
\begin{pmatrix}
\widehat{\psi} \\
\widehat{\psi_b} \\
\widehat{\frac{\partial \psi_b}{\partial x}}
\end{pmatrix},
\qquad (26)
$$

Equations (23)-(26) can be rewritten in a compact form

$$
\widehat{\frac{\partial^l \psi}{\partial x^l}} = \widehat{\mathcal{D}}_{lx}\widehat{\psi} + \widehat{k}_{lx}, \qquad (27)
$$

where the matrices $\widehat{\mathcal{D}}_{lx}$ ($l = \{1, 2, 3, 4\}$) consist of all but the last four columns of the product of two matrices on the right-hand side of (23) to (26), and $\widehat{k}_{lx}$ come from multiplying the vector $\left(\widehat{\psi_b}, \widehat{\frac{\partial \psi_b}{\partial x}}\right)^T$ by these last four columns. It is noted that $\widehat{k}_{lx}$ are the vectors of known quantities related to boundary conditions.

Since the discretization used has a structured form, the process of joining "local" 1D-IRBF approximations together (assemblage process) is quite straightforward. For a special case of rectangular domain, the IRBF approximations over a 2D domain can simply be constructed using the tensor direct product.

The fourth- and also third-order mixed derivatives are computed using the following relations

$$
\frac{\partial^4 \psi}{\partial^2 x \partial^2 y} = \frac{1}{2}\left[\frac{\partial^2}{\partial x^2}\left(\frac{\partial^2 \psi}{\partial y^2}\right) + \frac{\partial^2}{\partial y^2}\left(\frac{\partial^2 \psi}{\partial x^2}\right)\right], \qquad (28)
$$

$$
\frac{\partial^3 \psi}{\partial^2 x \partial y} = \frac{\partial^2}{\partial x^2}\left(\frac{\partial \psi}{\partial y}\right), \qquad (29)
$$

$$
\frac{\partial^3 \psi}{\partial x \partial y^2} = \frac{\partial^2}{\partial y^2}\left(\frac{\partial \psi}{\partial x}\right). \qquad (30)
$$

Expressions (28)-(30) reduce the computation of mixed derivatives to that of lower-

15

order pure derivatives for which IRBFNs involve integration with respect to x or y only. The additional work here is the computation of $\partial^2(F)/\partial x^2$ and $\partial^2(F)/\partial y^2$ where F is a derivative function of ψ (i.e. $\partial^2\psi/\partial y^2, \partial^2\psi/\partial x^2, \partial\psi/\partial y$ and $\partial\psi/\partial x$). It can be seen that the discretization of (5) requires the values of the mixed derivatives at the interior points. IRBFN-2s can be employed here to construct the approximations for $\partial^2(F)/\partial x^2$ and $\partial^2(F)/\partial y^2$. Both sets of centres and collocation points of these second-order networks consist of the interior nodes only.

The IRBF expressions for derivatives are now written in terms of the values of ψ at the interior points, and they already satisfy the boundary conditions. These nodal variable values are determined by forcing the approximate solution to satisfy the momentum equation at the interior points. Like the energy equation, the resultant system of algebraic equations here is of size $n_{ip} \times n_{ip}$, where n_{ip} is the number of interior points of the domain.

3.2.3 Solution procedures

An important feature of natural convection is that the temperature and velocity fields are closely coupled. The energy and momentum equations must be solved simultaneously to find the values of the temperature and stream function at discrete points within the domain. Due to the presence of convective terms, the obtained algebraic equations for the discrete solution are nonlinear. Two basic approaches are adopted here to handle this nonlinearity.

3.2.4 A steady-state solution coupled approach

All time derivative terms in the governing equations are dropped out. We employ the trust region dogleg techniques (e.g. [33]) to solve the discretized nonlinear

16

governing equations for the whole set of the variables. The main advantages of these techniques over the Gauss-Newton methods are that they are capable of handling the cases where the starting point is far from the solution and the Jacobian matrix is singular.

3.2.5   A time dependent decoupled approach

The nonlinear equation set is solved in a marching manner.

1. Guess initial values of T, ψ and their first-order spatial derivatives at time $t = 0$.

2. Discretize the governing equations in time using a first-order accurate finite-difference scheme, where the diffusive and convective terms are treated implicitly and explicitly, respectively.

3. Discretize the governing equations in space using 1D-IRBF schemes:
   Solve the energy equation (4) for T, and
   Solve the momentum equation (5) for ψ.
   The two equations are solved separately in order to keep matrix sizes to a minimum.

4. Check to see whether the solution has reached a steady state

$$CM = \frac{\sqrt{\sum_{i=1}^{n_{ip}} \left(\psi_i^{(k)} - \psi_i^{(k-1)} \right)^2}}{\sqrt{\sum_{i=1}^{n_{ip}} \left(\psi_i^{(k)} \right)^2}} < \epsilon, \tag{31}$$

   where k is the time level and ϵ is the tolerance.

5. If it is not satisfied, advance time step and repeat from step 2. Otherwise, stop the computation and output the results.

17

Each approach has its own particular strengths. For example, the former can be seen to be less parametric (no time steps specified here), while the latter allows the breakup of the problem into the solution of the energy equation and the solution of the momentum equation (two smaller subproblems at each iteration).

4   Numerical results

The present method is applied to the simulation of buoyancy-driven flow in annuli. A wide range of the Rayleigh number is considered. The computed solution at the lower and nearest value of Ra is taken to be the initial solution. The MQ-RBF width is simply chosen to be the grid size h.

4.1   Natural convection in a concentric annulus between two circular cylinders

Consider the natural convection between two concentric cylinders which are separated by a distance L, the inner cylinder heated and the outer cylinder cooled (Figure 1). A comprehensive review of this problem can be found in [1]. Most cases have been reported with $Pr = 0.7$ and $L/D_i = 0.8$, in which D_i is the diameter of the inner cylinder. These conditions are also employed in the present work. Kuehn and Goldstein [1] have also reported finite-difference results for $Ra = 10^2$ to $Ra = 7 \times 10^4$. Using the DQM, Shu [11] has provided the benchmark special results for values of the Rayleigh number in the range of 10^2 to 5×10^4.

One typical quantity associated with this type of flow is the average equivalent

conductivity denoted by $\bar{k}_{eq}$. This quantity is defined as ([1,11])

$$\bar{k}_{eq} = \frac{-\ln(D_o/D_i)}{2\pi} \oint \frac{\partial T}{\partial n} ds \tag{32}$$

in which D_o is the diameter of the outer cylinder.

The stream function and its normal derivative are set to zero along the inner and outer cylinders. The temperature is held at $T = 1$ at the inner cylinder and $T = 0$ at the outer cylinder. We employ a number of uniform Cartesian grids, namely $11 \times 11, 21 \times 21, \cdots, 61 \times 61$, to study the behaviour of convergence of the method. Both coupled and decoupled approaches are applied here to solve the nonlinear equation set. The codes are written using MATLAB. For the coupled approach, it takes about 5 to 10 iterations to get a converged solution. For the decoupled approach, much more iterations are required as shown in Figure 3. However, a single iteration of the decoupled approach consumes much less CPU time than that of the coupled approach. Overall, the decoupled approach is more efficient than the coupled approach. For example, in the case of simulating the flow at $Ra = 10^4$ using a grid of 41×41, the decoupled approach is about 9.2 times faster than the coupled approach.

The condition numbers of the system matrix associated with the harmonic (13) and biharmonic (20) operators in the governing equations (4) and (5) are reported in Table 1.

Results concerning $\bar{k}_{eq}$ together with those of Kuehn and Goldstein [1] and of Shu [11] for various Rayleigh numbers from 10^2 to 7×10^4 are presented in Tables 2-8. It can be seen that there is a good agreement between these numerical solutions. For each Rayleigh number, the convergence of the average equivalent conductivity with grid refinement is fast, e.g. the solution k_{eqo} for the last two Rayleigh numbers (i.e.

19

$Ra = 10^4$ and $Ra = 5 \times 10^4$) converges as $O(h^{2.71})$ and $O(h^{3.36})$ in which h is the grid spacing (errors are computed relative to the spectral results). Variations of the local equivalent conductivity on the inner and outer cylinder surfaces using a grid of 51×51 for $Ra = 10^3$ and $Ra = 5 \times 10^4$ are shown in Figures 4 and 5, respectively. It can be seen that they are compared well with those of Kuehn and Goldstein [1].

Figure 6 shows the streamlines and isotherms of the flow for $Ra = \{10^3, 6 \times 10^3, 5 \times 10^4, 7 \times 10^4\}$ using a grid of 51×51. Each plot contains 21 contour lines whose levels vary linearly from the minimum to maximum values. The plots look reasonable in comparison with those of the FD and DQ methods.

4.2 Natural convection in a concentric annulus between an outer square cylinder and an inner circular cylinder

There are relatively few papers on the numerical study of natural convection heat transfer from a heated inner circular cylinder to its cooled square enclosure. Moukalled and Acharya [34] have employed a control volume-based numerical technique to solve the governing equations in a boundary-fitted coordinate system. The curvilinear grid that maps the physical domain to a uniform computational domain is obtained by numerically solving a set of Poisson equations related to the two coordinate systems. Shu and Zhu [27] have introduced a super elliptic function to represent the outer square boundary in order to compute the geometrical parameters in an analytic manner. It can be seen that the transformation of the physical into the computational coordinates for this problem is much more complicated than that for the previous problem. On the other hand, the present technique solves the governing equations in the Cartesian coordinate system and therefore does not requires any extra work when changing the shape of the domain here. A typical discretization is shown in Figure 7.

An aspect ratio of $R/L = 0.2$ (L: the side length of the outer square cylinder), $Pr = 0.71$ and $Ra = \{10^4, 5 \times 10^4, 10^5, 5 \times 10^5, 10^6\}$ are considered here. Boundary conditions are specified in the same way as those of the previous problem. Calculations are conducted on three uniform Cartesian grids of 41×41, 51×51 and 61×61. The obtained results are presented in the forms of streamlines, isotherms (Figure 8) and the average Nusselt number (Table 9). In Figure 8, each plot contains 21 contour lines whose levels vary linearly from the minimum to maximum values. Following the work of Moukalled and Acharya [34], the local heat transfer coefficient is defined as

$$h = -\frac{k \partial T / \partial n}{\Delta T}, \tag{33}$$

where k is the thermal conductivity. The average Nusselt number (the ratio of the temperature gradient at the wall over a reference temperature gradient) is computed by

$$\bar{N}u = \frac{\bar{h}}{k}, \tag{34}$$

where $\bar{h} = -\oint \frac{\partial T}{\partial n} ds$. In Moukalled and Acharya [34], the computational domain is taken as one-half of the physical domain owing to the symmetry about the vertical axis of the flow. The values of $\bar{N}u$ in the present work (Table 9) are divided by 2 for comparison purposes. It can be seen that the RBF results are in good agreement with those of Moukalled and Acharya [34] and of Shu and Zhu [27].

4.3 Discussion

4.3.1 Comparison with other discretization techniques

The present method has several advantages over the FDM [1], FVM [34] and DQM [11,27]: (i) no difficulties are added when the level of complexity of the geometry increases; (ii) Given a spatial discretization, the size of the discretized equation set

21

for the velocity field is reduced by half; (iii) the governing equations are retained in their Cartesian form. Numerical results have shown that the proposed method achieves a fast rate of convergence with grid refinement. On the hand, the present RBF matrices are unsymmetric and not as sparse as those yielded through the FDM and FVM.

4.3.2 Comparison with two-dimensional RBF-based approaches

Generally, a two-dimensional RBF approach (i.e. RBFs are defined over the entire 2D domain) is expected to yield more accurate results than a one-dimensional RBF approach (i.e. RBFs cover single grid lines). However, as shown by theoretical results, the former leads to the interpolation matrix whose condition number grows exponentially with decreasing separation distance [35]. As a result, in practice, one is able to apply a two-dimensional approach with a few hundred collocation points [36]. As shown earlier (Table 1), the condition number of the 1D-IRBF matrix associated with the harmonic operator is only in the range of $O(10^1)$ to $O(10^3)$ for grids with densities of 11×11 to 61×61. The proposed approach thus facilitates the use of much larger numbers of nodes. In the context of fluid flow problems, the solutions usually have very complex shapes and one would expect to use a sufficiently-large number of nodes for an accurate simulation. The present approach appears to be more attractive than the original approach for such classes of problems.

5 Concluding remarks

In this paper, we have successfully implemented a numerical scheme based on Cartesian grids and 1D-IRBFNs for the simulation of natural convection in annuli. The attractiveness of the present technique lies in the simplicity of the preprocessing,

the ease of implementation and the achievement of high Rayleigh-number solutions. This study further demonstrates the great potential of the RBF technique for solving complex fluid-flow problems.

ACKNOWLEDGEMENTS

REFERENCES

1. Kuehn TH, Goldstein RJ. An experimental and theoretical study of natural convection in the annulus between horizontal concentric cylinders. *Journal of Fluid Mechanics* 1976; **74**(4):695–719.

2. de Vahl Davis G. Natural convection of air in a square cavity: a bench mark numerical solution. *International Journal for Numerical Methods in Fluids* 1983; **3**:249–264.

3. Manzari MT. An explicit finite element algorithm for convection heat transfer problems. *International Journal of Numerical Methods for Heat & Fluid Flow* 1999; **9**(8):860–877.

4. Sammouda H, Belghith A, Surry C. Finite element simulation of transient natural convection of low-Prandtl-number fluids in heated cavity. *International Journal of Numerical Methods for Heat & Fluid Flow* 1999; **9**(5):612–624.

5. Glakpe EK, Watkins CB, Cannon JN. Constant heat flux solutions for natural convection between concentric and eccentric horizontal cylinders. *Numerical Heat Transfer* 1986; **10**:279–295.

6. Kaminski DA, Prakash C. Conjugate natural convection in a square enclosure: effect of conduction in one of the vertical walls. *International Journal for Heat and Mass Transfer* 1986; **29**(12):1979–1988.

7. Kitagawa K, Wrobel LC, Brebbia CA, Tanaka M. A boundary element formulation for natural convection problems. *International Journal for Numerical Methods in Fluids* 1988; **8**:139–149.

8. Hribersek M, Skerget L. Fast boundary-domain integral algorithm for the computation of incompressible fluid flow problems. *International Journal for Numerical Methods in Fluids* 1999; **31**:891–907.

9. Power H, Mingo R. The DRM sub-domain decomposition approach for two-dimensional thermal convection flow problems. *Engineering Analysis with Boundary Elements* 2000; **24**:121–127.

10. Le Quere P. Accurate solutions to the square thermally driven cavity at high Rayleigh number. *Computers & Fluids* 1991; **20**(1):29–41.

11. Shu C. Application of differential quadrature method to simulate natural convection in a concentric annulus. *International Journal for Numerical Methods in Fluids* 1999; **30**:977–993.

12. Liu GR, Gu YT. A point interpolation method for two-dimensional solids. *International Journal for Numerical Methods in Engineering* 2001; **50**(4):937–951.

13. Sarler B, Perko J, Chen CS. Radial basis function collocation method solution of natural convection in porous media. *International Journal of Numerical Methods for Heat & Fluid Flow* 2004; **14**(2):187–212.

14. Johansen H, Colella P. A Cartesian Grid Embedded Boundary Method for Poisson's Equation on Irregular Domains. *Journal of Computational Physics*

1998; **147**(1):60–85.

15. Ye T, Mittal R, Udaykumar HS, Shyy W. An accurate cartesian grid method for viscous incompressible flows with complex immersed boundaries. *Journal of Computational Physics* 1999; **156**(2):209–240.

16. Gibou F, Fedkiw RP, Cheng L-T, Kang M. A second-order-accurate symmetric discretization of the Poisson equation on irregular domains. *Journal of Computational Physics* 2002; **176**(1):205–227.

17. Jomaa Z, Macaskill C. The embedded finite difference method for the Poisson equation in a domain with an irregular boundary and Dirichlet boundary conditions. *Journal of Computational Physics* 2005; **202**(2):488–506.

18. Rosatti G, Cesari D, Bonaventura L. Semi-implicit,semi-Lagrangian modelling for environmental problems on staggered Cartesian grids with cut cells. *Journal of Computational Physics* 2005; **204**(1):353–377.

19. Schwartz P, Barad M, Colella P,Ligocki T. A Cartesian grid embedded boundary method for the heat equation and Poisson's equation in three dimensions. *Journal of Computational Physics* 2006; **211**(2):531–550.

20. Kansa EJ. Multiquadrics- A scattered data approximation scheme with applications to computational fluid-dynamics-II. Solutions to parabolic, hyperbolic and elliptic partial differential equations. *Computers and Mathematics with Applications* 1990; **19**(8/9):147–161.

21. Fasshauer GE. Solving partial differential equations by collocation with radial basis functions. In *Surface Fitting and Multiresolution Methods*, Le Mehaute A, Rabut C, Schumaker LL (Editors). Vanderbilt University Press: Nashville, TN, 1997; 131–138.

22. Zerroukat T, Power H, Chen CS. A numerical method for heat transfer problems using collocation and radial basis functions. *International Journal for Numerical Methods in Engineering* 1998; **42**:1263–1278.

23. Kansa EJ, Hon YC. Circumventing the ill-conditioning problem with multiquadric radial basis functions: applications to elliptic partial differential equations. *Computers and Mathematics with Applications* 2000; **39**:123–137.

24. Mai-Duy N, Tran-Cong T. Numerical solution of differential equations using multiquadric radial basis function networks. *Neural Networks* 2001; **14**(2):185–199.

25. Sarler B. A radial basis function collocation approach in computational fluid dynamics. *Computer Modeling in Engineering & Sciences* 2005; **7**(2):185–194.

26. Mai-Duy N, Tran-Cong T. A Cartesian-grid collocation method based on radial-basis-function networks for solving PDEs in irregular domains. *Numerical Methods for Partial Differential Equations* 2007; **23**:1192–1210.

27. Shu C, Zhu YD. Efficient computation of natural convection in a concentric annulus between an outer square cylinder and an inner circular cylinder. *International Journal for Numerical Methods in Fluids* 2002; **38**:429–445.

28. Ostrach S. Natural convection in enclosures. *Journal of Heat Transfer* 1988; **110**:1175–1190.

29. Madych WR, Nelson SA. Multivariate interpolation and conditionally positive definite functions, II. *Mathematics of Computation* (1990); **54**(189):211–230.

30. Mai-Duy N, Tran-Cong T. Approximation of function and its derivatives using radial basis function networks. *Applied Mathematical Modelling* 2003; **27**:197–220.

31. Roache PJ. *Computational Fluid Dynamics*. Hermosa Publishers: Albuquerque, 1980.

32. Mai-Duy N, Tran-Cong T. Numerical solution of Navier-Stokes equations using multiquadric radial basis function networks. *International Journal for Numerical Methods in Fluids* 2001; **37**:65–86.

33. More JJ, Sorensen DC. Computing a trust region step. *SIAM Journal on Scientific and Statistical Computing* 1983; **3**:553–572.

34. Moukalled F, Acharya S. Natural convection in the annulus between concentric horizontal circular and square cylinders. *Journal of Thermophysics and Heat Transfer* 1996; **10**(3):524–531.

35. Fasshauer GE. *Meshfree Approximation Methods With Matlab*. Interdisciplinary Mathematical Sciences - Vol. 6. World Scientific Publishers: Singapore, 2007.

36. Li J, Hon YC. Domain decomposition for radial basis meshless methods. *Numerical Methods for Partial Differential Equations* 2004; **20**:450–462.

Table 1: Circular cylinders: Condition numbers of the RBF matrices associated with the harmonic and biharmonic operators.

Grid	cond($\mathcal{L}_2 T$)	cond($\mathcal{L}_4 \psi$)
11×11	1.3×10^1	7.4×10^1
21×21	1.2×10^2	5.0×10^3
31×31	3.3×10^2	3.3×10^4
41×41	5.1×10^2	7.9×10^4
51×51	7.5×10^2	1.6×10^5
61×61	1.0×10^3	3.2×10^5

Table 2: Circular cylinders: Convergence of $\bar{k}_{eq}$ with grid refinement for the flow at $Ra = 10^2$.

Grid	Outer cylinder, k_{eqo}	Inner cylinder, k_{eqi}
11×11	0.969	0.972
21×21	0.994	0.989
31×31	0.997	0.997
41×41	0.999	0.999
FDM [1]	1.002	1.000
DQM [11]	1.001	1.001

Table 3: Circular cylinders: Convergence of $\bar{k}_{eq}$ with grid refinement for the flow at $Ra = 10^3$.

Grid	Outer cylinder, k_{eqo}	Inner cylinder, k_{eqi}
11×11	1.133	1.046
21×21	1.072	1.069
31×31	1.078	1.077
41×41	1.080	1.079
51×51	1.081	1.080
FDM [1]	1.084	1.081
DQM [11]	1.082	1.082

Table 4: Circular cylinders: Convergence of $\bar{k}_{eq}$ with grid refinement for the flow at $Ra = 3 \times 10^3$.

Grid	Outer cylinder, k_{eqo}	Inner cylinder, k_{eqi}
11×11	1.745	1.200
21×21	1.365	1.378
31×31	1.387	1.386
41×41	1.391	1.390
51×51	1.393	1.393
FDM [1]	1.402	1.404
DQM [11]	1.397	1.397

Table 5: Circular cylinders: Convergence of $\bar{k}_{eq}$ with grid refinement for the flow at $Ra = 6 \times 10^3$.

Grid	Outer cylinder, k_{eqo}	Inner cylinder, k_{eqi}
31×31	1.698	1.702
41×41	1.704	1.705
51×51	1.709	1.709
61×61	1.711	1.711
FDM [1]	1.735	1.736
DQM [11]	1.715	1.715

Table 6: Circular cylinders: Convergence of $\bar{k}_{eq}$ with grid refinement for the flow at $Ra = 10^4$.

Grid	Outer cylinder, k_{eqo}	Inner cylinder, k_{eqi}
41×41	1.961	1.967
51×51	1.969	1.971
61×61	1.973	1.973
FDM [1]	2.005	2.010
DQM [11]	1.979	1.979

Table 7: Circular cylinders: Convergence of $\bar{k}_{eq}$ with grid refinement for the flow at $Ra = 5 \times 10^4$.

Grid	Outer cylinder, k_{eqo}	Inner cylinder, k_{eqi}
41×41	3.089	3.045
51×51	2.936	2.946
61×61	2.922	2.941
FDM [1]	2.973	3.024
DQM [11]	2.958	2.958

Table 8: Circular cylinders: Convergence of $\bar{k}_{eq}$ with grid refinement for the flow at $Ra = 7 \times 10^4$.

Grid	Outer cylinder, k_{eqo}	Inner cylinder, k_{eqi}
41×41	3.465	3.254
51×51	3.241	3.187
61×61	3.167	3.174
FDM [1]	3.226	3.308

Table 9: Circular and square cylinders: Convergence of the average Nu number on the outer square cylinder with grid refinement for different Ra values.

Grid	Ra				
	10^4	5×10^4	10^5	5×10^5	10^6
41×41	3.223	4.040	4.883	7.129	8.684
51×51	3.224	4.045	4.895	7.433	8.700
61×61	3.224	4.047	4.901	7.488	8.726
DQM [27]	3.24		4.86		8.90
FVM [34]	3.331		5.08		9.374
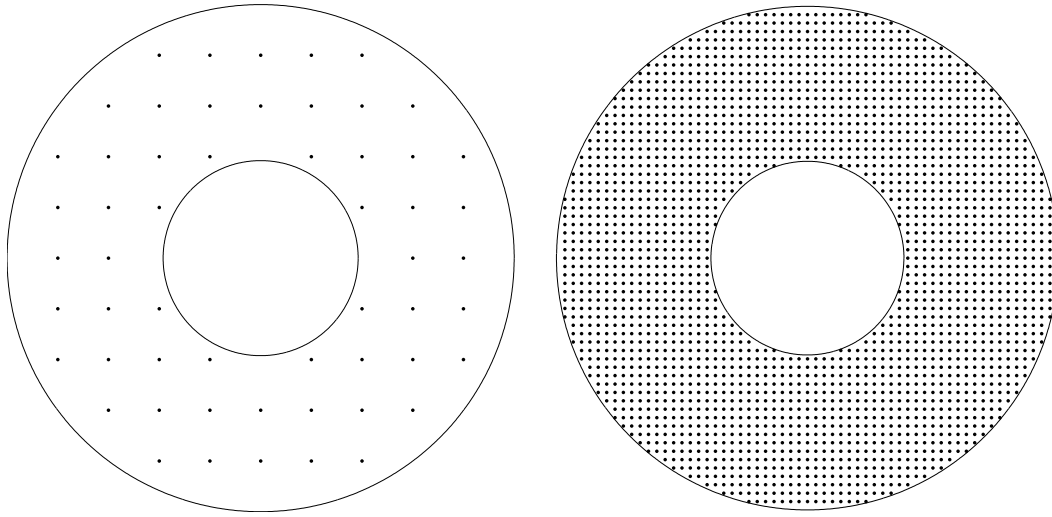
Figure 1: Circular cylinders: Computational domain and discretizations: 11×11 (left) and 61×61 (right).
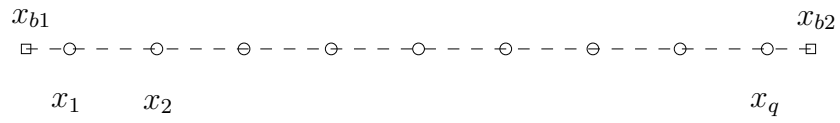
Figure 2: Points on a grid line consist of interior points x_i ($\circ$) and boundary points x_{bi} ($\square$).
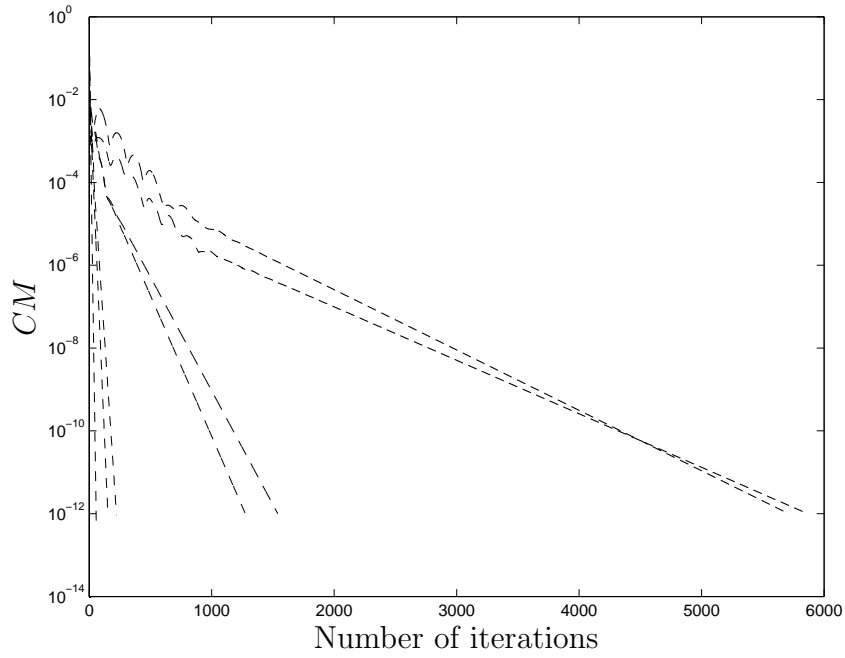
Figure 3: Circular cylinders, 61×61, decoupled approach: Iterative convergence. Time steps used are 0.5 for $Ra = \{10^2, 10^3, 3 \times 10^3\}$, 0.1 for $Ra = \{6 \times 10^3, 10^4\}$, and 0.05 for $Ra = \{5 \times 10^4, 7 \times 10^4\}$. The values of CM become less than 10^{-12} when the numbers of iterations reach 58, 154, 224, 1276, 1541, 5711 and 5867 for $Ra = \{10^2, 10^3, 3 \times 10^3, 6 \times 10^3, 10^4, 5 \times 10^4, 7 \times 10^4\}$, respectively.
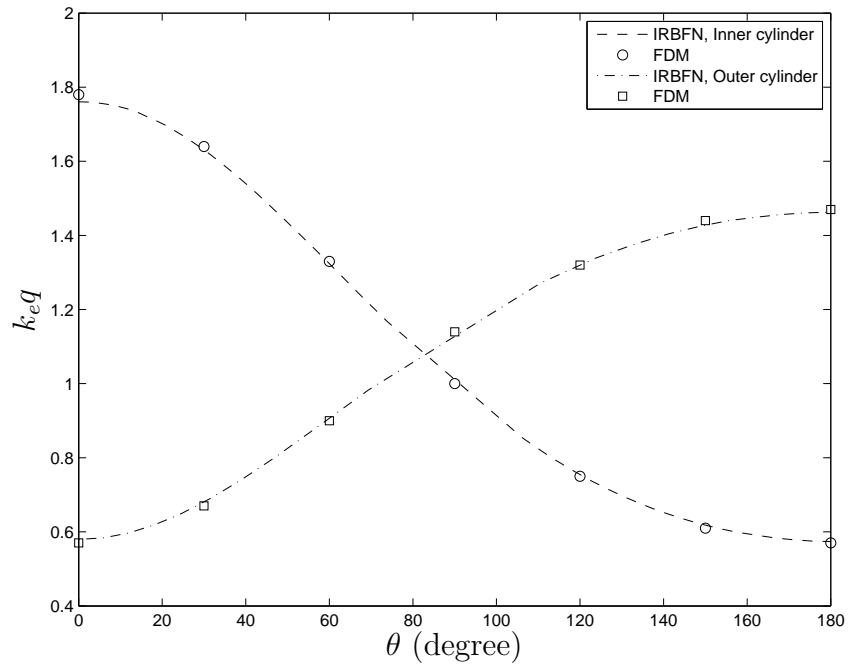
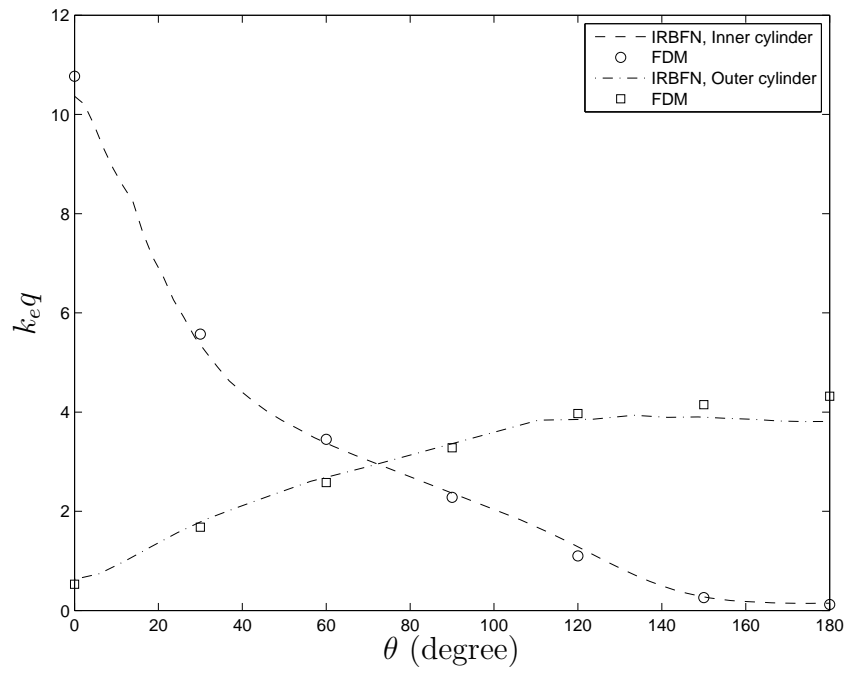Figure 4: Circular cylinders: Local equivalent conductivities for $Ra = 10^3$ by 1D-IRBFN and FDM.

Figure 5: Circular cylinders: Local equivalent conductivities for $Ra = 5 \times 10^4$ by 1D-IRBFN and FDM.

$$Ra = 10^3$$

$$Ra = 6 \times 10^3$$
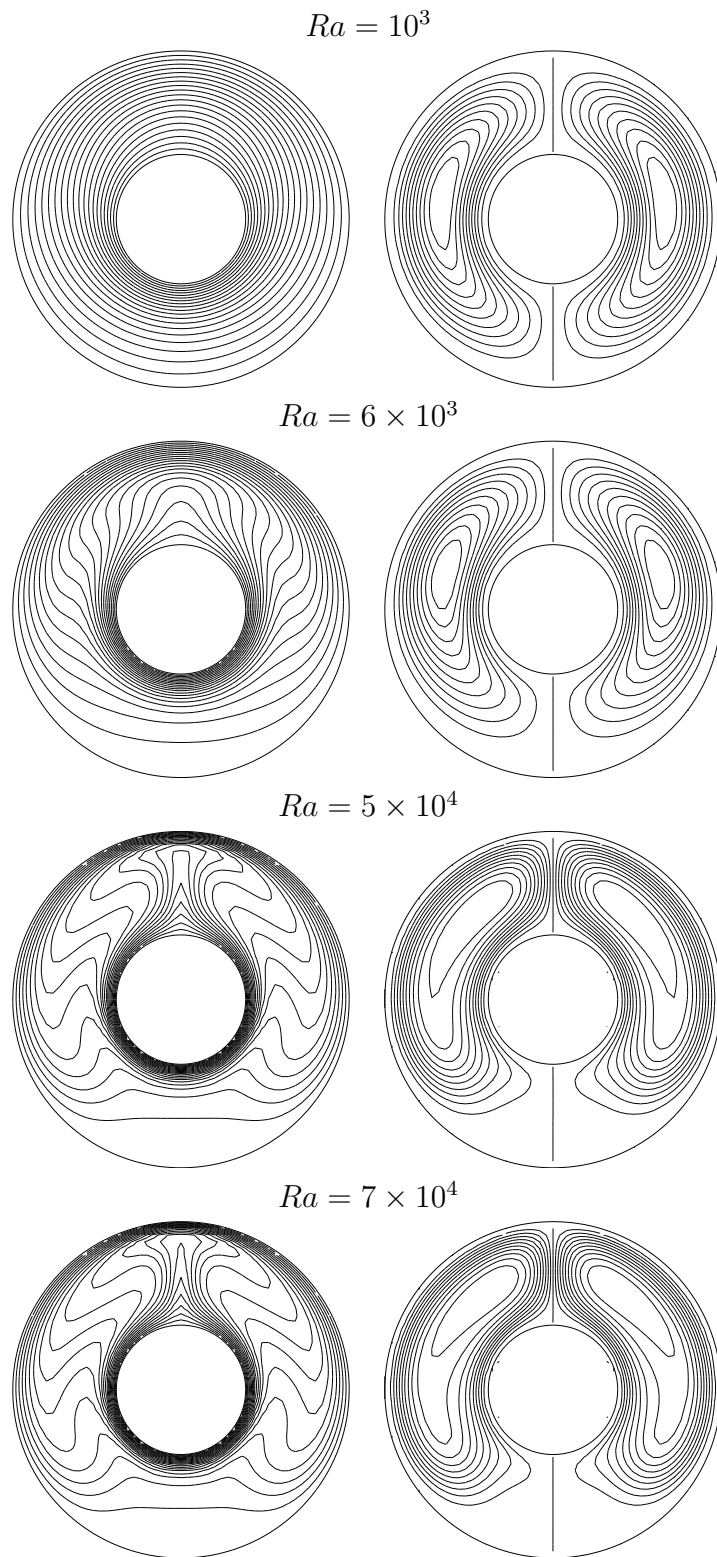

$$Ra = 5 \times 10^4$$

$$Ra = 7 \times 10^4$$

Figure 6: Circular cylinders: Contour plots of temperature (left) and stream function (right) for four different Rayleigh numbers using a grid of 51×51.
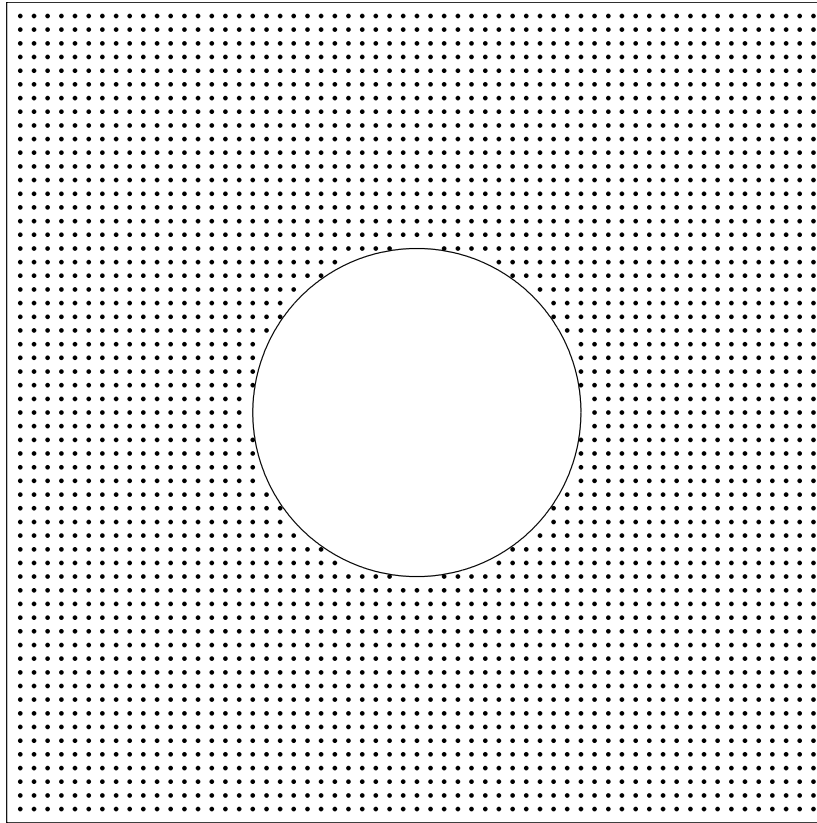
Figure 7: Circular and square cylinders: Computational domain and discretization.

$$Ra = 5 \times 10^4$$

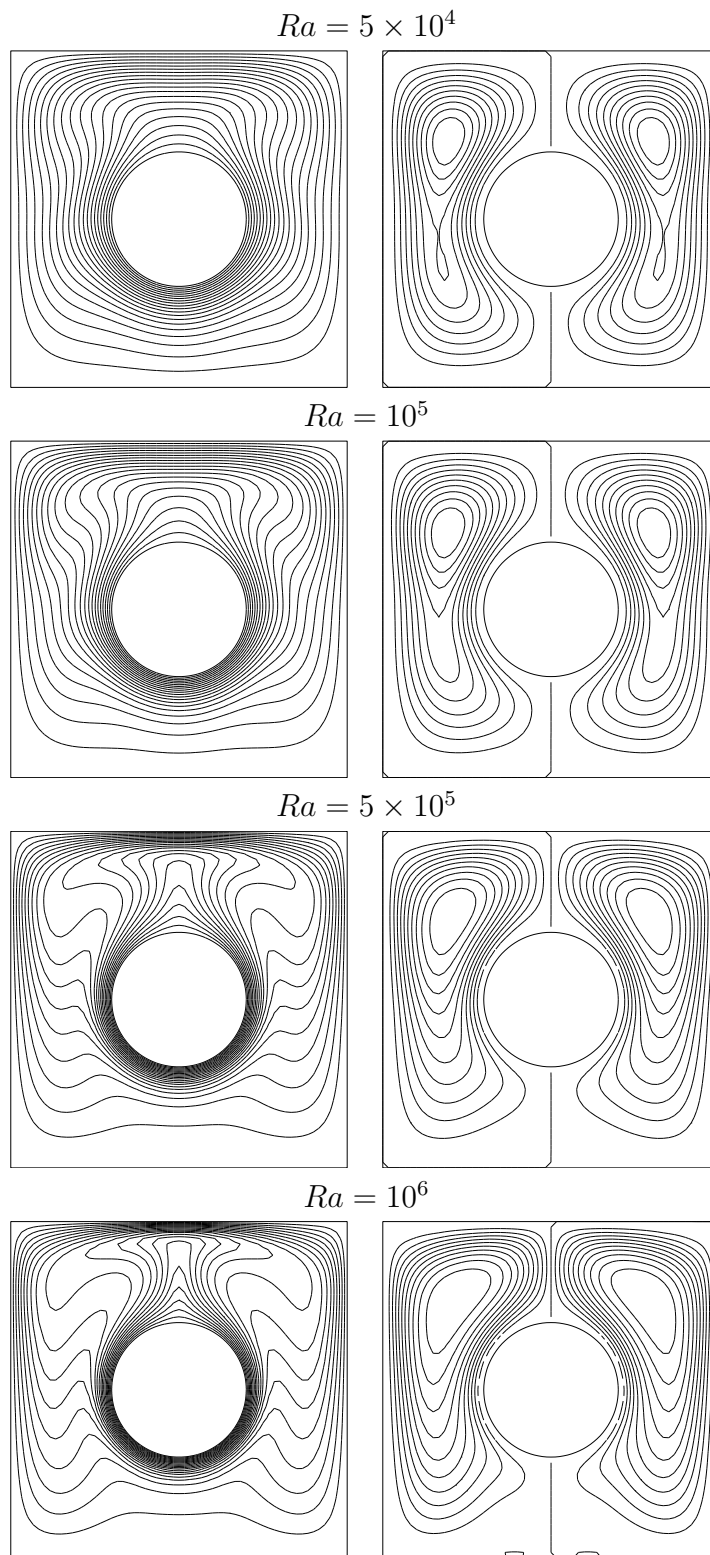$$Ra = 10^5$$

$$Ra = 5 \times 10^5$$

$$Ra = 10^6$$

Figure 8: Circular and square cylinders: Contour plots of temperature (left) and stream function (right) for four different Rayleigh numbers using a grid of 61×61.

44